PAPER

Check for updates

Crystal lattice and electronic and transport properties of Janus ZrSiSZ$_2$ (Z = N, P, As) monolayers by first-principles investigations

Nguyen P. Q. Anh,[a] Nguyen T. Hiep, [ID] [bc] D. V. Lu, [ID] [d] Cuong Q. Nguyen, [ID] [bc] Nguyen N. Hieu [ID] [bc] and Vo T. T. Vi [ID] *[e]

From the extending requirements for using innovative materials in advanced technologies, it is necessary to explore new materials for relevant applications. In this work, we design new two-dimensional (2D) Janus ZrSiSZ$_2$ (Z = N, P, As) monolayers and investigate their crystal lattice and dynamic stability by using density functional theory investigations. The two stable structures of ZrSiSP$_2$ and ZrSiSAs$_2$ are then systematically examined for thermal, energetic, and mechanical stability, and electronic and transport properties. The calculation results demonstrate that both the ZrSiSP$_2$ and ZrSiSAs$_2$ monolayers have good thermal stability at room temperature and high energetic/mechanical stabilities for experimental synthesis. The studied structures are found to be in-direct semiconductors. Specifically, with moderate band-gap energies of 1.04 to 1.29 eV for visible light absorption, ZrSiSP$_2$ and ZrSiSAs$_2$ can be considered potential candidates for photovoltaic applications. The applied biaxial strains and external electric fields slightly change the band-gap energies of the monolayers. We also calculate the carrier mobilities for the transport properties based on the deformation potential method. Due to the lower effective masses, the carrier mobilities in the *x* direction are higher than those in the *y* direction. The carrier mobilities of the ZrSiSP$_2$ and ZrSiSAs$_2$ monolayers are anisotropic not only in transport directions but also for the electrons and holes. We believe that the results of our work may stimulate further studies to explore more new 2D Janus monolayers with novel properties of the MA$_2$Z$_4$ family materials.

1 Introduction

Since the exploration of graphene,[1] two-dimensional (2D) materials have received extensive attention from researchers because of their extraordinary chemical and physical features. Numerous 2D materials have been investigated and reported such as transition metal oxides,[2] antinonene,[3] bismuthene,[4] phosphorene,[5] MXenes,[6] transition metal chalcogenides,[7,8] *etc.* Specifically, the emergence of 2D Janus monolayers as a novel class of 2D materials with extraordinary properties caused by their asymmetric structures has been intensely studied recently.[9] Based on the first principles calculations, many efforts have also been made to explore the potential

applications of these materials in optoelectronics,[10,11] nano-electronics,[12,13] thermoelectrics,[14] sensors,[15] and catalysis.[16,17]

Besides theoretical studies, some 2D Janus materials were successfully synthesized by experiments. For example, Janus graphene as an asymmetrically modified singled-layer was first prepared by Zhang and co-workers. The fabrication was carried out by using a two-step functionalization with a flexible macroscopic mediator of a poly(methyl methacrylate) film.[18] For transition-metal dichalcogenides, based on controlling the sulfurization process of MoSe$_2$, Zhang *et al.* fabricated 2D Janus SMoSe monolayers. They used chemical vapor deposition to grow MoSe$_2$ flakes, and then the top Se layer was substituted with vaporized sulfur during sulfurization at a high temperature of 800 °C.[19] Lin and co-workers presented the fabrication of Janus WSSe monolayers by pulsed laser deposition. The top and bottom S layer of the WS$_2$ monolayer was selectively and completely replaced by selenium by selenization at 300 °C. Thus, the high quality WSSe monolayers can be formed by implantation and recrystallization processes at low temperatures.[20] Recently, a new group of 2D materials known as the MA$_2$Z$_4$ family with M corresponding to the transition metal, A referring to Si/Ge, and Z being N/P/As has received growing interest.[21–23] The MA$_2$Z$_4$ monolayers were found to have good stabilities, tunable electronic properties, remarkable optical

[a]Faculty of Electrical, Electronics and Materials Technology, University of Sciences, Hue University, Hue 530000, Vietnam

[b]Institute of Research and Development, Duy Tan University, Da Nang 550000, Vietnam

[c]Faculty of Natural Sciences, Duy Tan University, Da Nang 550000, Vietnam

[d]Faculty of Physics, The University of Danang – University of Science and Education, Da Nang 550000, Vietnam

[e]Faculty of Basic Sciences, University of Medicine and Pharmacy, Hue University, Hue 530000, Vietnam. E-mail: vothituyetvi@hueuni.edu.vn

absorption, external quantum efficiencies, and excellent conductivity.[24–26] 2D $MoSi_2N_4$ material, a member of the MA_2Z_4 family was first fabricated by chemical vapor deposition. Hong *et al.* added Si during the growth of the 2D Mo_2N layer at 1080 °C on the Cu/Mo substrates to form the $MoSi_2N_4$ monolayer.[27] This successful experimental deposition motivated more studies on the MA_2Z_4 family and its derivatives.

Inspired by the attractive properties of these MA_2Z_4 materials, in this work, we design new Janus $ZrSiSZ_2$ (Z = N, P, As) monolayers with an optimized crystal lattice by using density functional theory (DFT). The phonon dispersion spectra of all three structures are obtained to test their dynamic stability. Then the two stable $ZrSiSP_2$ and $ZrSiSAs_2$ monolayers are examined for thermal stability based on *ab initio* molecular dynamics (AIMD) simulations. We also calculate cohesive energy and elastic constants to check the energetic and mechanical stabilities of the materials for experimental synthesis. Besides, the band-gap energies and band structures are also studied using Heyd–Scuseria–Ernzerhof (HSE06) and Perdew–Burke–Ernzerhof (PBE) methods. Moreover, we apply biaxial strains and external electric fields to $ZrSiSP_2$ and $ZrSiSAs_2$ for evaluation of their impacts on the band structures. The transport properties are also examined by calculating the effective masses as well as the carrier mobilities.

2 Computational method

Herein, the Vienna *ab initio* simulation package[28,29] was used for first principles investigations based on density functional theory (DFT). For calculations of the phonon dispersions, we built a 6 × 6 × 1 supercell and used the frozen-phonon technique in the PHONOPY code.[30] *Ab initio* molecular dynamics (AIMD) simulation was carried out at 500 K within 20 ps to examine the thermodynamic stability.[31] The electronic-exchange-correlation functional was performed by utilizing the Perdew–Burke–Ernzerhof (PBE) functional.[32] Also, we added the spin–orbit coupling

(SOC) to the self-consistent calculations in the calculations for the electronic structures.[33] To calculate more accurate bandgap energies and band diagrams of the studied monolayers, we also used the Heyd–Scuseria–Ernzerhof (HSE06) method.[34] The plane-wave basic cut-off energy was chosen to be 500 eV. In addition, we adopted the semi-empirical DFT-D3 method[35] to describe the interactions between the weak van der Waals (vdW) interlayers. The Brillouin zone (BZ) was tested by using the Monkhorst–Pack scheme[36] using a (15 × 15 × 1) *k*-point grid. The criterion of energy convergence was set to be 10^{-6} eV. The maximum force on atoms of the optimized structures was less than 10^{-3} eV Å^{-1}. A large vacuum space of 20 Å was inserted in the vertical direction to reduce the interactions of the adjacent periodic images. The deformation potential (DP) method was utilized to calculate the mobility of carriers.[37]

3 Results and discussion

3.1 Crystal lattice and stabilities

To study the geometric configuration, we build the crystal structures of $ZrSiSZ_2$ as depicted in Fig. 1. The top view with a rhombus unit cell shows that the Zr and X atoms are located at the center of hexagonal structures (Fig. 1(a)). From the side view, the $ZrSiSZ_2$ monolayers are composed by stacking in order five atomic layers of S–Zr–X–Si–X (only one element in each layer). We can also say that the geometry of the monolayers is made up of a Zr–S bilayer stacked on the top of the Si–X_2 sublayer along the z axis. Due to the electronegativity and radius differences of the atoms, a reflection symmetry breaking appears in these studied structural configurations, resulting in 2D Janus structures of the $ZrSiSZ_2$ monolayers.

After relaxation, the structural parameters of lattice constants (*a*), monolayer thicknesses (Δ*h*), as well as chemical bond-lengths of S–Zr, Zr–X, Si–X(1), and Si–X(2) (*d*) are calculated and presented in Table 1. The *a* and Δ*h* of the $ZrSiSZ_2$ monolayers vary from 3.14 Å to 3.69 Å and 5.14 Å to 6.51 Å, respectively. It is easy to observe that both the *a* and Δ*h* values increase with increasing atomic number in the periodicity of the X atoms. The Zr–X and Si–X bond-lengths of Zr and Si with X atoms (d_{Zr-X} and d_{Si-X}) also gradually increase from the $ZrSiSN_2$ to $ZrSiSP_2$ and $ZrSiSAs_2$, similar to the trend with increasing of lattice constants and monolayer thicknesses.

Next, the phonon dispersion spectra of $ZrSiSZ_2$ are obtained to check their dynamic stability. The obtained results are presented in Fig. 2. The phonon spectra of the $ZrSiSZ_2$ monolayers contain fifteen vibration modes with twelve optical modes and three acoustic modes because the primitive cell has five atoms
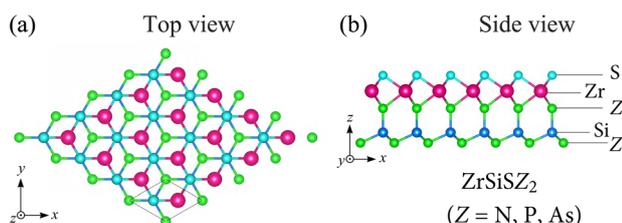

Fig. 1 (a) Top and (b) side views of Janus $ZrSiSZ_2$ (Z = N, P, As) monolayers.

Table 1 Lattice constant *a* (Å), monolayer thickness Δ*h* (Å), bond-lengths *d* (Å) of S–Zr, Zr–X, Si–X(1), and Si–X(2), cohesive energy E_{coh} (eV per atom), elastic constants C_{ij} (N m^{-1}), Young modulus Y_{2D} (N m^{-1}), Poisson's ratio ν_{2D}, and band-gaps E_g (eV) from PBE, PBE + SOC, and HSE06 methods of $ZrSiSZ_2$ monolayers

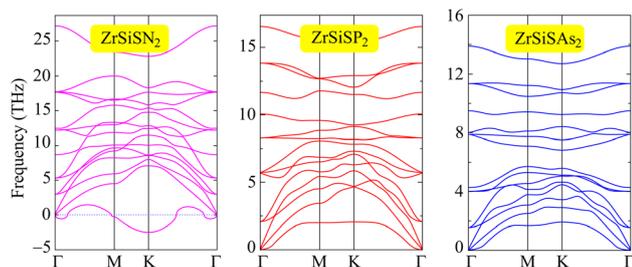|	A	Δh	d_{S-Zr}	d_{Zr-X}	$d_{Si-X(1)}$	$d_{Si-X(2)}$	E_{coh}	C_{11}	C_{12}	C_{66}	Y_{2D}	ν_{2D}	E_g^{PBE}	$E_g^{PBE+SOC}$	E_g^{HSE06}
$ZrSiSN_2$	3.14	5.14	2.51	2.18	1.75	1.87	—	—	—	—	—	—	—	—	—
$ZrSiSP_2$	3.59	6.26	2.54	2.63	2.21	2.29	−6.44	141.01	42.29	49.36	128.33	0.30	0.70	0.69	1.29
$ZrSiSAs_2$	3.69	6.51	2.55	2.73	2.32	2.39	−6.09	132.48	42.02	45.23	119.15	0.32	0.50	0.44	1.04

Fig. 2 Phonon dispersions of ZrSiN$_2$, ZrSiP$_2$, and ZrSiAs$_2$ monolayers.
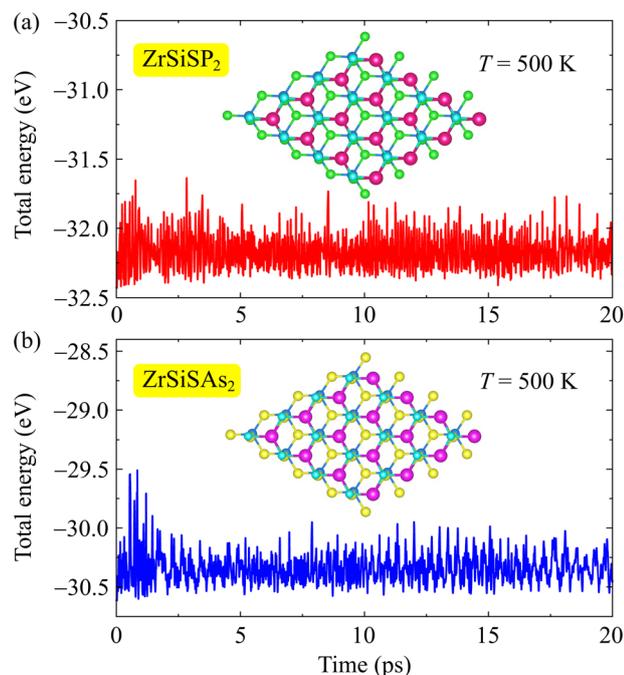

Fig. 3 AIMD simulations of the time-dependent total energy fluctuation of (a) ZrSiP$_2$ and (b) ZrSiAs$_2$ monolayers at $T = 500$ K. Insets show the crystal structures of the studied materials at the end of the AIMD simulations.

of Zr, Si, and S, and two X atoms. However, we can observe the presence of an imaginary frequency in the ZrSiN$_2$ monolayer, especially at the K point. Whereas, there are only positive phonon frequencies in ZrSiP$_2$ and ZrSiAs$_2$ without any negative frequency, suggesting that these monolayers are more dynamically stable than ZrSiN$_2$. Therefore, in the following section, we only investigate and discuss the properties of the ZrSiP$_2$ and ZrSiAs$_2$ monolayers.

We further examine the thermodynamic stability of ZrSiP$_2$ and ZrSiAs$_2$ by using AIMD simulations at $T = 500$ K within 20 ps. The total energy fluctuations dependent on heating time and the crystal structures after testing are shown in Fig. 3. We can see only a little fluctuation, the total energy is quite stable during the AIMD test. After heating for 20 ps, the lattice structures of ZrSiP$_2$ and ZrSiAs$_2$ are still robust. No structural transitions or bond breaking is observed, demonstrating that

these two monolayers are thermally stable. It is noted that the heat of formation of a material is also an important parameter for the thermodynamic stability test.[38] The thermodynamic stability requires that the formation energy of a material must be below the convex hull.[38] In this work, we only test the thermodynamic stability of the ZrSiP$_2$ and ZrSiAs$_2$ monolayers based on the AIMD simulations.

To characterize the energetic stability of ZrSiP$_2$ and ZrSiAs$_2$ for experimental synthesis, we calculate the cohesive energy (E_{coh}) using the following equation:

$$E_{\mathrm{coh}} = \frac{E_{\mathrm{tot}} - \left(N_{\mathrm{Zr}}E_{\mathrm{Zr}} + N_{\mathrm{Si}}E_{\mathrm{Si}} + N_{\mathrm{S}}E_{\mathrm{S}} + N_{\mathrm{P/As}}E_{\mathrm{P/As}}\right)}{N_{\mathrm{Zr}} + N_{\mathrm{Si}} + N_{\mathrm{S}} + N_{\mathrm{P/As}}}, \quad (1)$$

where E_{tot} denotes the total energy in the unit-cell of the ZrSiP$_2$ and ZrSiAs$_2$ monolayers. E_{Zr}, E_{Si}, E_{S}, $E_{\mathrm{P/As}}$, N_{Zr}, N_{Si}, N_{S}, and $N_{\mathrm{P/As}}$ correspond to the single atom energies and total atom number of Zr, Si, S and P/As, respectively. The obtained cohesive energy values are -6.44 eV per atom for ZrSiP$_2$ and -6.09 eV per atom for ZrSiAs$_2$, as shown in Table 1. The negative E_{coh} suggests that the two monolayers have energetically favorable structures. Besides, the low E_{coh} values (about -6 eV per atom) are similar to that of other 2D Janus materials[39] and lower than that of the recently reported STiSiP$_2$ (-4.78 eV per atom) and STiSiAs$_2$ (-4.49 eV per atom).[40] Thus, the ZrSiP$_2$ and ZrSiAs$_2$ monolayers have high energetic stability for the experimental synthesis.

In addition, to investigate the mechanical stability according to the criterion of Born–Huang, the elastic constants C_{ij} are estimated. In principle, four elastic constants need to be calculated C_{11}, C_{12}, C_{22}, and C_{66}. However, we have $C_{66} = (C_{11} - C_{12})/2$ and $C_{22} = C_{11}$ because of the hexagonal symmetry of the ZrSiP$_2$ and ZrSiAs$_2$ structures. Therefore, we only have to calculate C_{11} and C_{12} by polynomial fitting of the dependence of applied strain (in the range of -1.5% to 1.5%) on the elastic energy.[41] The attained C_{ij} values are presented in Table 1. It is found that the two monolayers have elastic constants that obey the criterion of Born–Huang for mechanical stability with positive C_{11} values and $C_{11} - C_{12} > 0$.[42,43] Therefore, the ZrSiP$_2$ and ZrSiAs$_2$ structures are mechanically stable.

From the elasticity theory, Young's modulus Y_{2D} as well as Poisson's ratio ν_{2D} are achieved by utilizing the elastic constants as follows:[43]

$$Y_{2D} = \frac{C_{11}^2 - C_{12}^2}{C_{11}}, \quad (2)$$

$$\nu_{2D} = \frac{C_{12}}{C_{11}}. \quad (3)$$

As summarized in Table 1, the calculated Y_{2D} value for ZrSiP$_2$ is 128.33 N m^{-1} and ZrSiAs$_2$ is 119.15 N m^{-1}. These values are comparable to that of STiSiP$_2$ (130.57 N m^{-1}) and STiSiAs$_2$ (115.96 N m^{-1})[40] and much smaller than the Y_{2D} values of other reported Janus materials of graphene (336 N m^{-1}),[44] MoGe$_2$P$_4$ (183.76 N m^{-1}), and MoSi$_2$P$_4$ (204.80 N m^{-1}),[45] This ensures that the ZrSiP$_2$ and ZrSiAs$_2$ monolayers have higher mechanical flexibility. At the same time, the ν value of ZrSiP$_2$ is
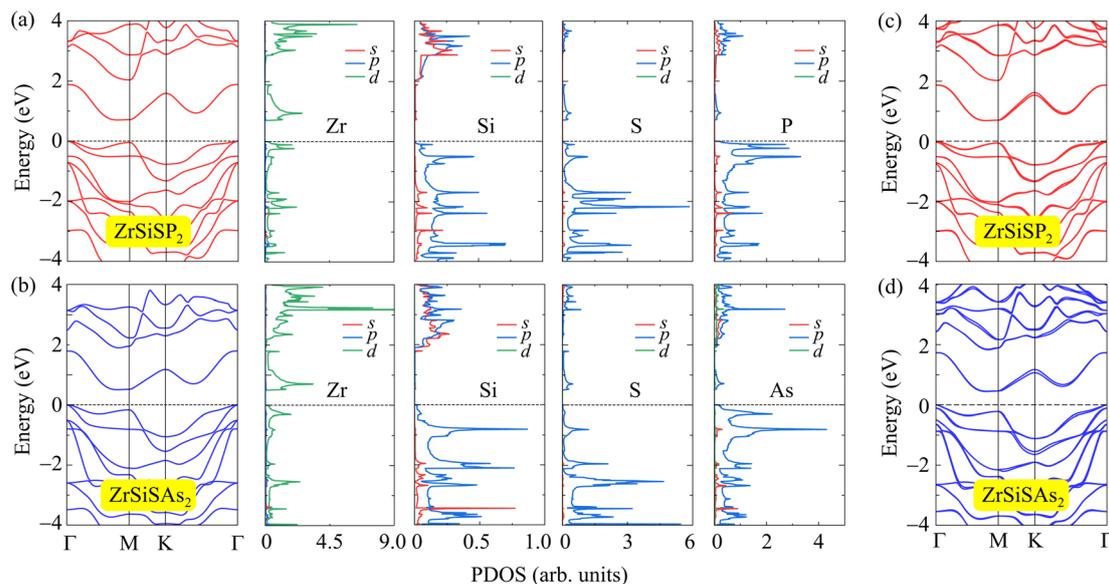
Fig. 4 The PBE band structures and corresponding PDOS of 2D Janus (a) ZrSiSP$_2$ and (b) ZrSiSAs$_2$ monolayers. The calculated band structures of (c) ZrSiSP$_2$ and (d) ZrSiSAs$_2$ using the PBE + SOC method.
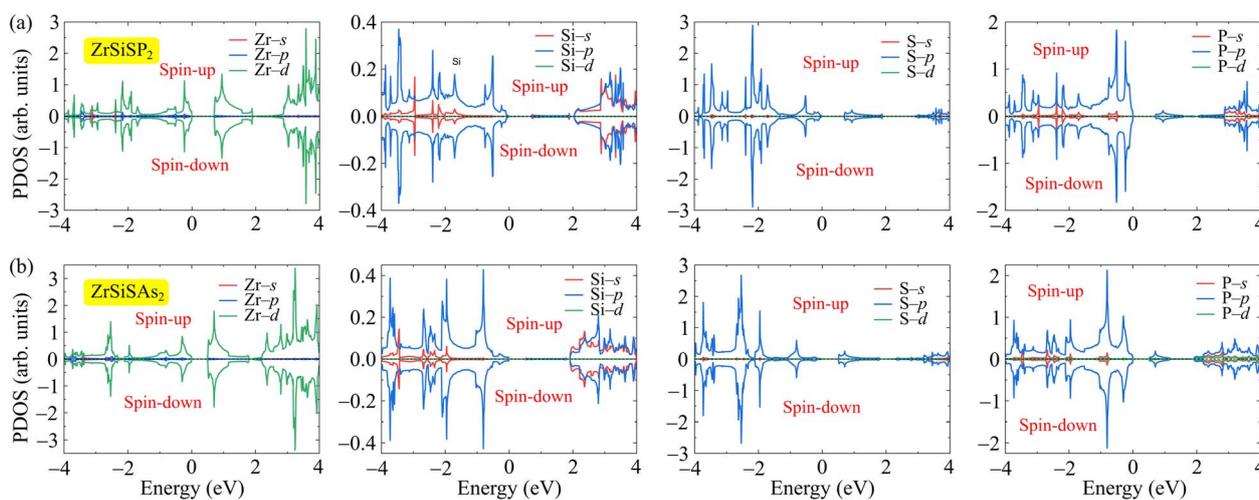

Fig. 5 Spin-polarized PDOS of 2D Janus (a) ZrSiSP$_2$ and (b) ZrSiSAs$_2$ monolayers.

0.30 and ZrSiSAs$_2$ is 0.32, which is consistent with the smaller lattice constant a of the ZrSiSP$_2$ monolayer. These attained ν values are larger than that of the other Janus materials.[21,46–48]

3.2 Electronic properties

Additionally, we explore the electronic properties of ZrSiSP$_2$ and ZrSiSAs$_2$ for electronic applications. Fig. 4(a and b) show the band structures examined by the PBE method along the Γ–M–K–Γ direction in the first Brillouin zone. The two monolayers are exhibited as indirect band-gap semiconductors, with the maximum valence band (VBM) located on the Γ-line and the minimum conduction band (CBM) located at the ΓM-line. As listed in Table 1, the band-gap value of ZrSiSP$_2$ is 0.70 eV and ZrSiSAs$_2$ is 0.50 eV. We also obtain the partial density of states (PDOS) to elucidate the contribution to electronic bands of the

orbitals as presented in Fig. 4(a) and (b). The p orbitals of Si, S, and P/As show a remarkable contribution to the valence band formation. Whereas the Zr-d orbital mainly contributes to the conduction band and S-p and P/As-p orbitals only provide small contributions to the CBM.

It is noted that the influences of the SOC effect on the compounds based on heavier elements are significant. In Fig. 4(c and d), we show the band structures of ZrSiSP$_2$ and ZrSiSAs$_2$ calculated by the PBE + SOC method. It is shown that when the SOC effect was taken into account, the spin degeneracy at the band edges is removed. Also, the band gap of the studied structures is reduced due to the SOC effect. The PBE + SOC band gaps of ZrSiSP$_2$ and ZrSiSAs$_2$ monolayers are found, respectively, to be 0.69 and 0.44 eV, which are slightly smaller than those calculated by the PBE method as listed in Table 1. In
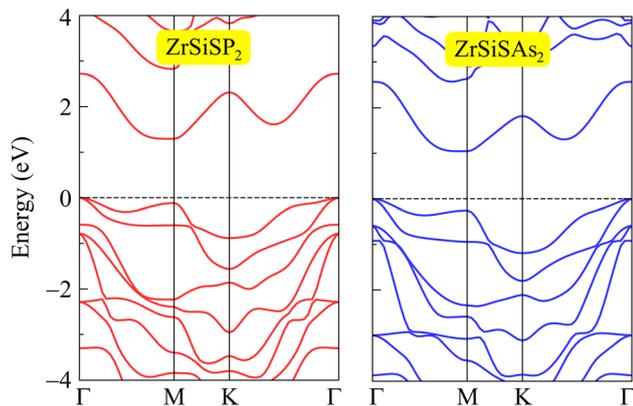
Fig. 6 Calculated band structures of $ZrSiSP_2$ and $ZrSiSAs_2$ using the HSE06 approach.

Fig. 5, we show the spin-polarized PDOS of the studied systems. It is found that the PDOS with the spin-up and spin-down configurations is the same for both $ZrSiSP_2$ and $ZrSiSAs_2$. This suggests that $ZrSiSP_2$ and $ZrSiSAs_2$ are non-magnetic materials.

The calculated band gaps of semiconductors from the PBE method are generally underestimated.[49] Then, the hybrid functional[34] or GW approximation[50] are often chosen to correct the band gap of the semiconductors or insulators. These are the methods considered suitable to obtain accurate results of the semiconductor band gap.[38] In this work, we use the HSE06 approach to correct the band gaps of $ZrSiSP_2$ and $ZrSiSAs_2$ monolayers. From Fig. 6, we can see that the band structures of $ZrSiSP_2$ and $ZrSiSAs_2$ from the HSE06 approach are similar to those from the PBE calculation results, with indirect-semiconductor characteristics. The HSE06 band-gaps of the monolayers are larger with 1.29 eV for $ZrSiSP_2$ and 1.04 eV for

$ZrSiSAs_2$. In addition to the electronic applications for semiconductor materials with these moderate band-gap energies for the absorption of visible light from the solar spectrum, $ZrSiSP_2$ and $ZrSiSAs_2$ are promising candidates for photovoltaic applications (Fig. 6).

Furthermore, we clarify the influences of biaxial strains ε_b on the band structure of the studied $ZrSiSP_2$ and $ZrSiSAs_2$. Herein, the ε_b is expressed as $\varepsilon_b = (a - a_0)/a_0 \times 100\%$, where a and a_0 correspond to the distorted and undistorted lattice constants, respectively. The band structures of $ZrSiSP_2$ and $ZrSiSAs_2$ under a compressive strain of -6% to a tensile strain of $+6\%$ are presented in Fig. 7. It is easy to observe that the applied strains have a significant influence on the band-gap energy of the monolayers. The conduction bands are shifted far from the Fermi level when the strains increase, leading to an increase in the band-gap energies. Besides, for $ZrSiSP_2$, the valence band edge positions are also moved from the Γ-line to the M-line by applied compressive strains. However, the $ZrSiSP_2$ monolayer still exhibits indirect band-gap semiconductor characteristics because the CBM is located at the ΓM-path. The calculated band-gap energy values dependent on the strains are shown in Fig. 9(a). We can see that the description graphs of both $ZrSiSP_2$ and $ZrSiSAs_2$ have similar trends with increasing band-gap values from the compressive to tensile strains.

Besides the biaxial strains, we also investigate the impacts of an applied electric field (E) on the $ZrSiSP_2$ and $ZrSiSAs_2$ band structures. E with a strength of -4 to $+4$ V nm^{-1} is applied on the studied monolayers. The negative and positive values are applied, respectively, opposite to and along the z-direction. The band-gap energies are decreased for the larger E as illustrated in Fig. 8. The shape of band structures for both $ZrSiSP_2$ and $ZrSiSAs_2$ monolayers do not change much. However, the electric fields show a slight shift of the conduction band edge, resulting
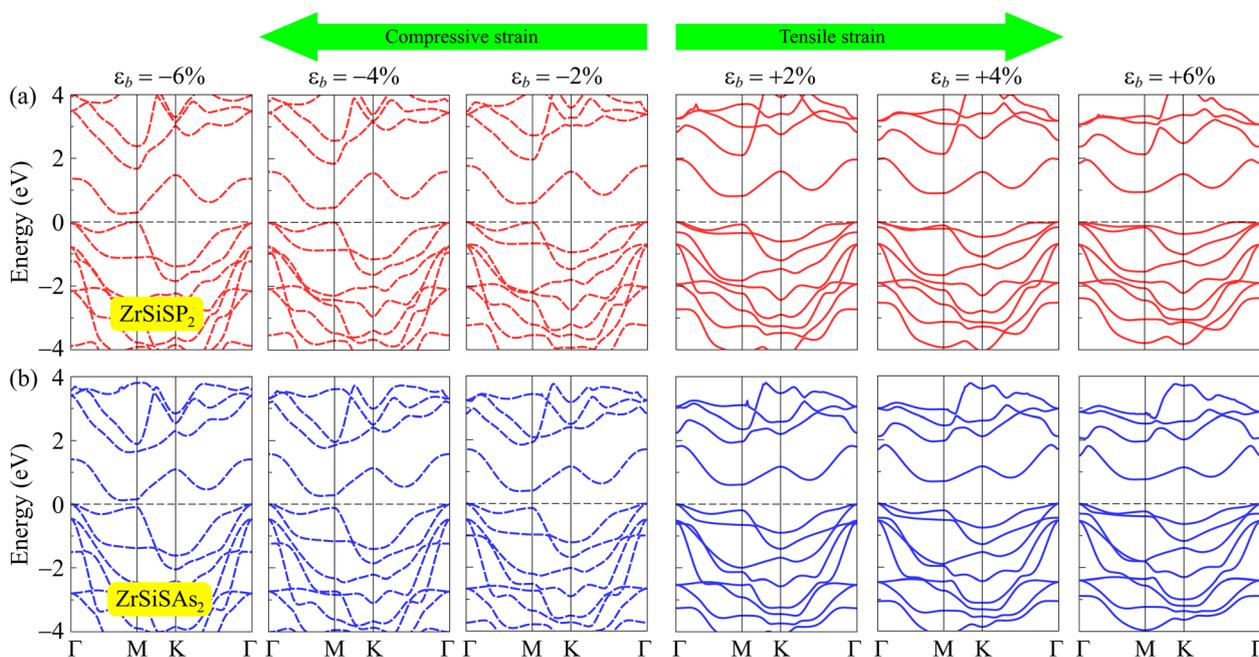

Fig. 7 Band structures of (a) $ZrSiSP_2$ and (b) $ZrSiSAs_2$ monolayers under compressive and tensile biaxial strains ε_b.
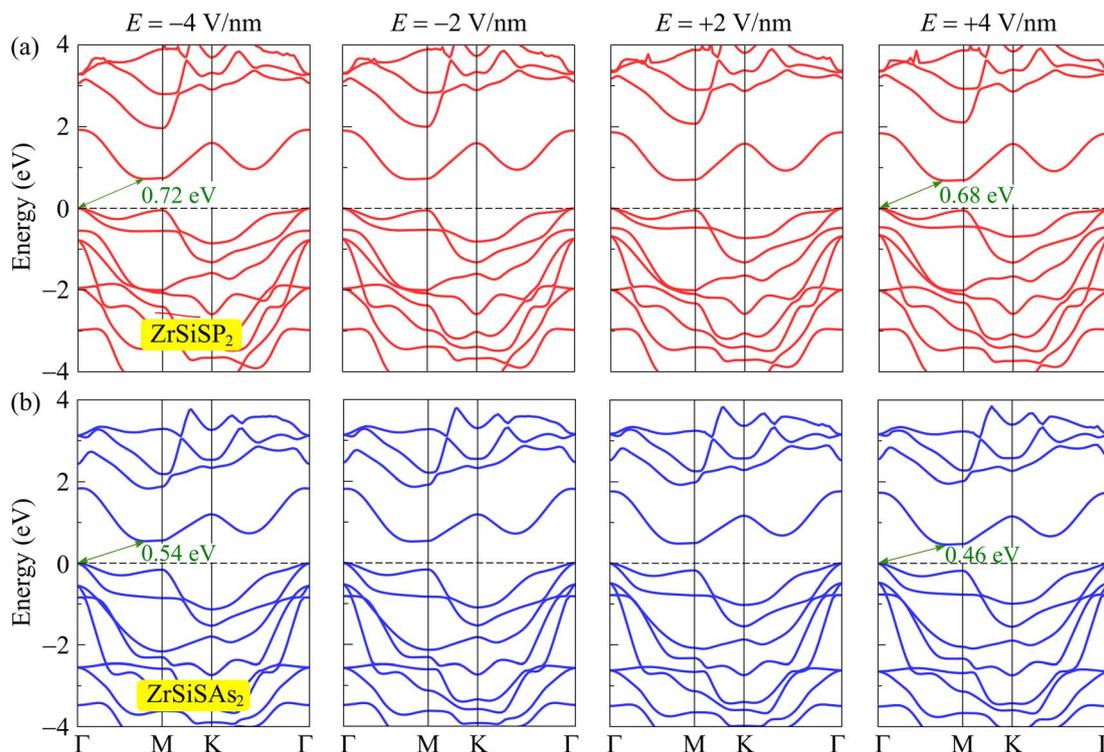
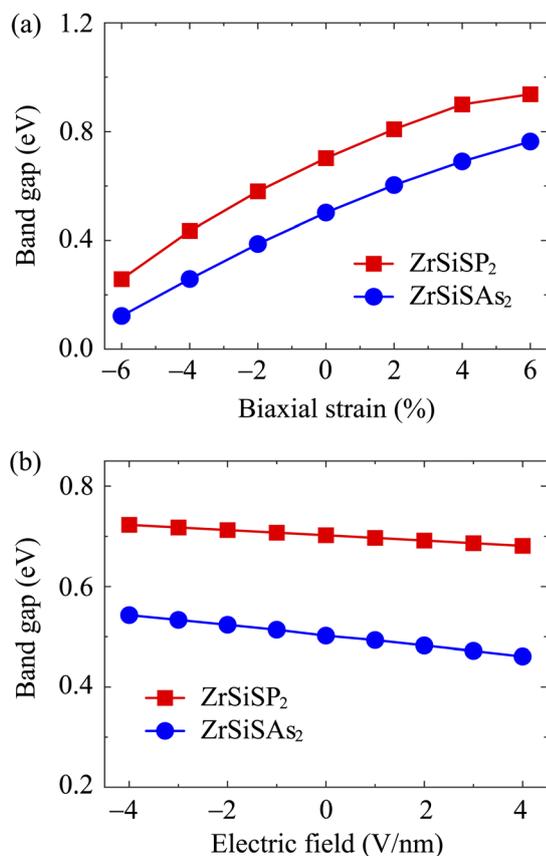**Fig. 8** Band structures of (a) ZrSiSP$_2$ and (b) ZrSiSAs$_2$ at several values of E.

Fig. 9 Dependence of bandgaps of ZrSiSP$_2$ and ZrSiSAs$_2$ on the biaxial strains (a) and electric fields (b).

in lower band-gap energies from 0.72 to 0.68 eV for ZrSiSP$_2$, and 0.54 to 0.46 eV for the ZrSiSAs$_2$ monolayer. Fig. 9(b) shows the band-gap values as a function of the applied E of the two monolayers.

3.3 Transport properties

In order to confirm the promising electronic applications of the studied materials, in this part, we investigate the transport properties of the ZrSiSP$_2$ and ZrSiSAs$_2$ monolayers. Based on the DP approximation, the carrier mobilities μ_{2D} can be estimated as follows:[37]

$$\mu_{2D} = \frac{e\hbar^3 C_{2D}}{k_B T m^* \overline{m} E_d^2},$$ (4)

where $\hbar$ and k_B correspond to the reduced Planck and Boltzmann constants, respectively. e refers to the charge of the electron. m^* and $\overline{m} = \sqrt{m_x^* m_y^*}$ are, respectively, the carrier and average effective masses. T refers to the ambient temperature of 300 K. E_d denotes DP constant and C_{2D} is the elastic modulus.

The effective masses m^* of electrons and holes which describe their response to E and directly affect the carrier mobility μ can be attained using the following expression:

$$m^* = \hbar^2 \left[\frac{\partial^2 E(k)}{\partial k^2} \right]^{-1},$$ (5)

where $E(k)$ corresponds to the energy of carriers in the band edges at a k wave-vector. According to eqn (5), the flatter band dispersions can lead to smaller $\partial^2 E(k)/\partial k^2$, resulting in a larger

Table 2 Effective masses m^* of electrons and holes (m_0: the mass of a free electron), elastic modulus C_{2D} (N m^{-1}), DP constants E_d (eV), and carrier mobilities μ (cm^2 V^{-1} s^{-1}) of the studied ZrSiSP$_2$ and ZrSiSAs$_2$ along the x/y transport directions

		m_x^*	m_y^*	C_{2D}^x	C_{2D}^y	E_d^x	E_d^y	μ_x	μ_y
Electron	ZrSiSP$_2$	1.17	5.05	189.69	189.71	−5.32	−3.75	49.99	23.57
	ZrSiSAs$_2$	1.36	5.93	171.45	171.46	−4.90	−3.45	39.33	18.19
Hole	ZrSiSP$_2$	1.37	1.60	189.69	189.71	−7.44	−7.44	36.09	30.89
	ZrSiSAs$_2$	1.41	1.43	171.45	171.46	−6.91	−6.91	38.15	37.62
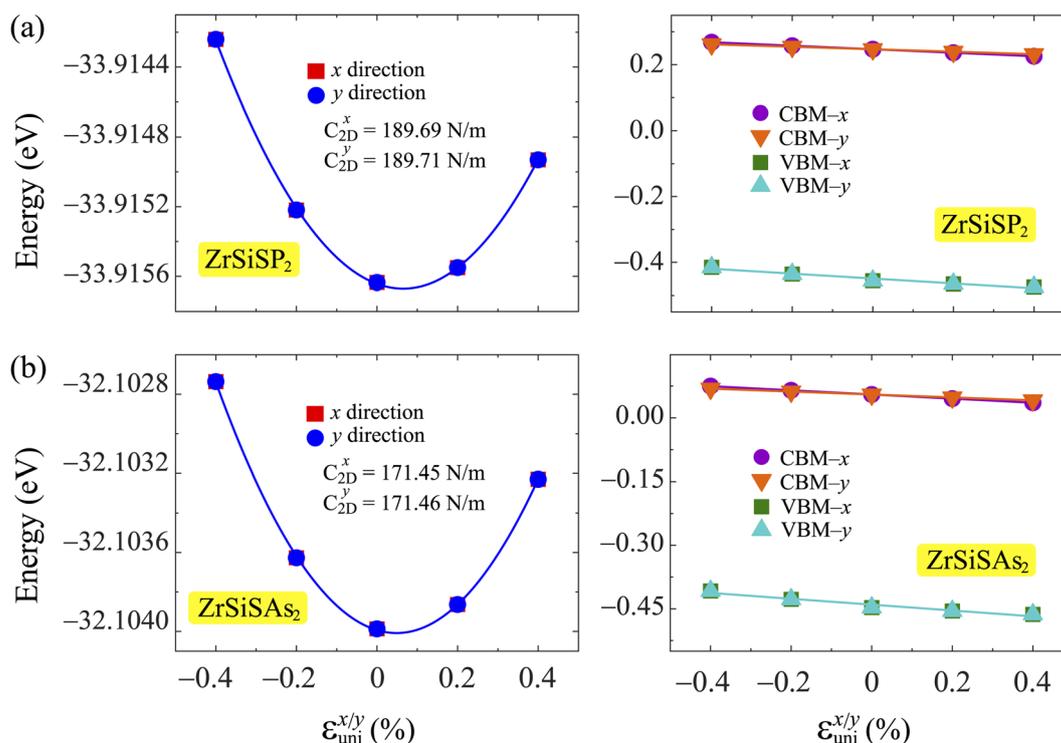
Fig. 10 The strain-dependence $\varepsilon_{uni}^{x/y}$ of the total energies and CBM/VBM energies of (a) ZrSiSP$_2$, and (b) ZrSiSAs$_2$. The solid lines present the fitted data.

effective mass. Therefore, the band dispersions near valence and conduction bands have significant effects on the m^* values. Table 2 summarizes the calculated m^* in x and y directions of the electrons and holes. Generally, m_y^* values are larger than m_x^* for both the electrons and holes of the two monolayers.

The elastic modulus C_{2D} can be calculated by using:

$$C_{2D} = \frac{1}{\Omega_0} \frac{\partial^2 E_{tot}}{\partial \varepsilon_{uni}^2}, \qquad (6)$$

where ε_{uni}, Ω_0, and E_{tot} are the applied strains, optimized supercell area, and total energy in the x and y transport directions.

The DP constant E_d is defined by:

$$E_d = \frac{\Delta E_{edge}}{\varepsilon_{uni}}, \qquad (7)$$

where ΔE_{edge} refers to the changing energy at the valence and conduction band edges.

The VBM/CBM positions and the total energy shifting are evaluated along two in-plane directions within the applied

strains ε_{uni} of −0.4 to 0.4%. By fitting the dependence of band edge energies with strains, the C_{2D} and E_d values can be obtained.[51,52] The calculated shifting energies and VBM/CBM positions of the ZrSiSP$_2$ and ZrSiSAs$_2$ monolayers are presented in Fig. 10. We can see that the C_{2D} values are almost the same in the x and y directions, with only slight differences in the C_{2D}^x and C_{2D}^y from 189.69 to 198.71 N m^{-1} for ZrSiSP$_2$ and 171.45 to 171.46 N m^{-1} for ZrSiSAs$_2$, respectively. Besides, the positions of band edges are also independent of the two in-plane directions for the two monolayers. Table 2 lists our calculated values of the C_{2D} and E_d. The DP constants of ZrSiSP$_2$ and ZrSiSAs$_2$ in the x and y axes for the electrons are quite anisotropic. From eqn (4), we can attain the μ_{2D} by using the above calculated C_{2D}, m^* and E_d values as tabulated in Table 2. The carrier mobilities μ_x in the x direction of the two studied structures are larger than the carrier mobilities μ_y in the y direction. This is related to their effective masses, where m_x^* is lower than m_y^*. The electron mobility values of ZrSiSP$_2$ are also larger than the electron mobilities of ZrSiSAs$_2$, while the hole mobilities of ZrSiSAs$_2$ are larger than that of ZrSiSP$_2$. The hole mobilities of about 30 cm^2

V^{-1} s^{-1} of the studied monolayers are larger than the hole mobility values of the recently reported 2D Janus $STiSiP_2$ and $STiSiAs_2$ materials.[40] Thus, we can see that the carrier mobilities of $ZrSiSP_2$ and $ZrSiSAs_2$ are anisotropic not only in transport directions but also for the electrons and holes.

4 Concluding remarks

Hence, we have designed and studied the crystal lattice as well as the dynamic stability of the $ZrSiSZ_2$ (Z = N, P, As) monolayers using DFT calculations. Except for $ZrSiSN_2$ with the presence of an imaginary frequency in the phonon spectrum, the two $ZrSiSP_2$ and $ZrSiSAs_2$ structures are dynamically stable and have good thermal stability at room temperature and high energetic/ mechanical stabilities for the experimental synthesis. We then systematically examine the electronic and transport properties of these stable $ZrSiSP_2$ and $ZrSiSAs_2$ structures. The PBE and HSE06 results demonstrate that the two studied monolayers are in-direct semiconductors with band-gap energies of 1.04 to 1.29 eV for visible light absorption. These moderate band gaps are an advantage for photovoltaic applications of the $ZrSiSP_2$ and $ZrSiSAs_2$ materials. The impacts of external electric fields and applied biaxial strains on the band structures of the monolayers are investigated. It is found that the band-gaps are slightly decreased for a larger E while when the applied ε_b increases from the compressive to tensile strains, the band-gap energies also increase. For the transport properties, the effective masses and carrier mobilities are calculated based on the DP method. The calculations show that the carrier mobility values in the x direction of the two studied structures are larger than the carrier mobilities in the y direction related to their lower effective masses. The carrier mobilities of the $ZrSiSP_2$ and $ZrSiSAs_2$ monolayers are anisotropic not only in transport directions but also for the electrons and holes. We believe that our study may inspire further investigations and studies to explore more new 2D Janus materials with specific properties for relevant applications.

Conflicts of interest

There are no conflicts of interest to declare.

Acknowledgements

References

1 K. S. Novoselov, A. K. Geim, S. V. Morozov, D. Jiang, Y. Zhang, S. V. Dubonos, I. V. Grigorieva and A. A. Firsov, *Science*, 2004, **306**, 666.

2 F. Song, L. Bai, A. Moysiadou, S. Lee, C. Hu, L. Liardet and X. Hu, *J. Am. Chem. Soc.*, 2018, **140**, 7748–7759.

3 D. Singh, S. K. Gupta, Y. Sonvane and I. Lukačević, *J. Mater. Chem. C*, 2016, **4**, 6386–6390.

4 F. Yang, A. O. Elnabawy, R. Schimmenti, P. Song, J. Wang, Z. Peng, S. Yao, R. Deng, S. Song, Y. Lin, M. Mavrikakis and W. Xu, *Nat. Commun.*, 2020, **11**, 1088.

5 J. Pang, A. Bachmatiuk, Y. Yin, B. Trzebicka, L. Zhao, L. Fu, R. G. Mendes, T. Gemming, Z. Liu and M. H. Rummeli, *Adv. Energy Mater.*, 2017, **8**, 1702093.

6 Y. Gogotsi and B. Anasori, *ACS Nano*, 2019, **13**, 8491–8494.

7 G. Giuffredi, T. Asset, Y. Liu, P. Atanassov and F. D. Fonzo, *ACS Mater. Au*, 2021, **1**, 6–36.

8 Y. Dahiya, M. Hariram, M. Kumar, A. Jain and D. Sarkar, *Coord. Chem. Rev.*, 2022, **451**, 214265.

9 A. C. Riis-Jensen, T. Deilmann, T. Olsen and K. S. Thygesen, *ACS Nano*, 2019, **13**, 13354–13364.

10 T. Tan, X. Jiang, C. Wang, B. Yao and H. Zhang, *Adv. Sci.*, 2020, **7**, 2000058.

11 M. Zhao, Y. Hao, C. Zhang, R. Zhai, B. Liu, W. Liu, C. Wang, S. H. M. Jafri, A. Razaq, R. Papadakis, J. Liu, X. Ye, X. Zheng and H. Li, *Crystals*, 2022, **12**, 1087.

12 M. Dragoman, A. Dinescu and D. Dragoman, *Phys. Status Solidi A*, 2019, **216**, 1800724.

13 Z. Liu, H. Wang, J. Sun, R. Sun, Z. F. Wang and J. Yang, *Nanoscale*, 2018, **10**, 16169–16177.

14 F. Khan, H. Din, S. Khan, G. Rehman, M. Bilal, C. V. Nguyen, I. Ahmad, L.-Y. Gan and B. Amin, *J. Phys. Chem. Solids*, 2019, **126**, 304–309.

15 D. Tyagi, H. Wang, W. Huang, L. Hu, Y. Tang, Z. Guo, Z. Ouyang and H. Zhang, *Nanoscale*, 2020, **12**, 3535–3559.

16 F. R. Fan, R. Wang, H. Zhang and W. Wu, *Chem. Soc. Rev.*, 2021, **50**, 10983–11031.

17 Y. Zhu, L. Peng, Z. Fang, C. Yan, X. Zhang and G. Yu, *Adv. Mater.*, 2018, **30**, 1706347.

18 L. Zhang, J. Yu, M. Yang, Q. Xie, H. Peng and Z. Liu, *Nat. Commun.*, 2013, **4**, 1443.

19 J. Zhang, S. Jia, I. Kholmanov, L. Dong, D. Er, W. Chen, H. Guo, Z. Jin, V. B. Shenoy, L. Shi and J. Lou, *ACS Nano*, 2017, **11**, 8192–8198.

20 Y.-C. Lin, C. Liu, Y. Yu, E. Zarkadoula, M. Yoon, A. A. Puretzky, L. Liang, X. Kong, Y. Gu, A. Strasser, H. M. Meyer, M. Lorenz, M. F. Chisholm, I. N. Ivanov, C. M. Rouleau, G. Duscher, K. Xiao and D. B. Geohegan, *ACS Nano*, 2020, **14**, 3896–3906.

21 H. Yao, C. Zhang, Q. Wang, J. Li, Y. Yu, F. Xu, B. Wang and Y. Wei, *Nanomaterials*, 2021, **11**, 559.

22 X. Liu, H. Zhang, Z. Yang, Z. Zhang, X. Fan and H. Liu, *Phys. Lett. A*, 2021, **420**, 127751.

23 Y. Gao, J. Liao, H. Wang, Y. Wu, Y. Li, K. Wang, C. Ma, S. Gong, T. Wang, X. Dong, Z. Jiao and Y. An, *Phys. Rev. Appl.*, 2022, **18**, 034033.

24 H. Zhong, W. Xiong, P. Lv, J. Yu and S. Yuan, *Phys. Rev. B*, 2021, **103**, 085124.

25 W. Zhang, W. Yang, Y. Liu, Z. Liu and F. Zhang, *Front. Phys.*, 2022, **17**, 63509.

26 N. Mwankemwa, H.-E. Wang, T. Zhu, Q. Fan, F. Zhang and W. Zhang, *Results Phys.*, 2022, **37**, 105549.

27 Y.-L. Hong, Z. Liu, L. Wang, T. Zhou, W. Ma, C. Xu, S. Feng, L. Chen, M.-L. Chen, D.-M. Sun, X.-Q. Chen, H.-M. Cheng and W. Ren, *Science*, 2020, **369**, 670–674.

28 G. Kresse and J. Furthmüller, *Phys. Rev. B: Condens. Matter Mater. Phys.*, 1996, **54**, 11169–11186.

29 G. Kresse and J. Furthmüller, *Comput. Mater. Sci.*, 1996, **6**, 15–50.

30 A. Togo, L. Chaput and I. Tanaka, *Phys. Rev. B: Condens. Matter Mater. Phys.*, 2015, **91**, 094306.

31 S. Nosé, *J. Chem. Phys.*, 1984, **81**, 511.

32 J. P. Perdew, K. Burke and M. Ernzerhof, *Phys. Rev. Lett.*, 1996, **77**, 3865.

33 A. H. MacDonald, W. E. Picket and D. D. Koelling, *J. Phys. C: Solid State Phys.*, 1980, **13**, 2675.

34 J. Heyd, G. E. Scuseria and M. Ernzerhof, *J. Chem. Phys.*, 2003, **118**, 8207.

35 S. Grimme, J. Antony, S. Ehrlich and H. Krieg, *J. Chem. Phys.*, 2010, **132**, 154104.

36 H. J. Monkhorst and J. D. Pack, *Phys. Rev. B: Condens. Matter Mater. Phys.*, 1976, **13**, 5188–5192.

37 J. Bardeen and W. Shockley, *Phys. Rev.*, 1950, **80**, 72.

38 S. Haastrup, M. Strange, M. Pandey, T. Deilmann, P. S. Schmidt, N. F. Hinsche, M. N. Gjerding, D. Torelli, P. M. Larsen, A. C. Riis-Jensen, J. Gath, K. W. Jacobsen, J. J. Mortensen, T. Olsen and K. S. Thygesen, *2D Mater.*, 2018, **5**, 042002.

39 N. T. Hiep, N. P. Q. Anh, H. V. Phuc, C. Q. Nguyen, N. N. Hieu and V. T. T. Vi, *Phys. Chem. Chem. Phys.*, 2023, **25**, 8779–8788.

40 Z. Gao, X. He, W. Li, Y. He and K. Xiong, *Dalton Trans.*, 2023, **52**, 8322–8331.

41 K.-A. N. Duerloo, M. T. Ong and E. J. Reed, *J. Phys. Chem. Lett.*, 2012, **3**, 2871–2876.

42 R. C. Andrew, R. E. Mapasha, A. M. Ukpong and N. Chetty, *Phys. Rev. B: Condens. Matter Mater. Phys.*, 2012, **85**, 125428.

43 N. T. Hung, A. R. T. Nugraha and R. Saito, *J. Phys. D: Appl. Phys.*, 2018, **51**, 075306.

44 O. Leenaerts, H. Peelaers, A. D. Hernández-Nieves, B. Partoens and F. M. Peeters, *Phys. Rev. B: Condens. Matter Mater. Phys.*, 2010, **82**, 195436.

45 Y. Liu, C. Shao, W. Yu, Q. Gui, J. Robertson and Y. Guo, *Appl. Phys. Lett.*, 2022, **121**, 244105.

46 T. Cheng, H. Lang, Z. Li, Z. Liu and Z. Liu, *Phys. Chem. Chem. Phys.*, 2017, **19**, 23942–23950.

47 R. M. Meftakhutdinov and R. T. Sibatov, *Nanomaterials*, 2022, **12**, 3904.

48 A. Politano and G. Chiarello, *Nano Res.*, 2015, **8**, 1847–1856.

49 J. P. Perdew and M. Levy, *Phys. Rev. Lett.*, 1983, **51**, 1884–1887.

50 L. Hedin, *Phys. Rev.*, 1965, **139**, A796.

51 W. Wan, S. Zhao, Y. Ge and Y. Liu, *J. Phys.: Condens.Matter.*, 2019, **31**, 435501.

52 S.-D. Guo, W.-Q. Mu, Y.-T. Zhu, R.-Y. Han and W.-C. Ren, *J. Mater. Chem. C*, 2021, **9**, 2464–2473.